Rate-distortion estimation of 2-D non-separable filter banks based on quaternionic filter banks with JPEG2000 discrete wavelet transforms

Eugene V. Rybenkov
Department of Computer Engineering
Belarusian State University of
Informatics and Radioelectronics
Minsk, Belarus
rybenkov@bsuir.by, 0000-0003-4548-411X

Nick A. Petrovsky
Department of Computer Engineering
Belarusian State University of
Informatics and Radioelectronics
Minsk, Belarus
nick.petrovsky@bsuir.by, 0000-0001-5807-8685

***Abstract*—This paper presents the evaluation of lossless-to-lossy transforms, such as quaternion algebra based pairwise-mirror-image (PMI) symmetric frequency responses (LP PMI Q-PUFB) filter bank and convenient discrete wavelet transforms used in industrial image compression standards: 5/3 (lossless mode only) and 9/7 (lossy mode only). Generalized image compression framework was developed, which main aim is to provide equal conditions in the terms of quantization and entropy coding. Rate distortion curves were obtained on the PSNR, DSIMM and SSIM metrics, Bjøntegaard delta was computed. Experimental results are provided for test images.**

***Index Terms*—filter bank, quaternion, discrete wavelet transform**

I. INTRODUCTION

Filter banks are essential components of the signal processing and have a wide variety of applications, including compression, communication, denoising, and feature extraction [1], [2]. In image processing, two-dimensional filter banks are utilized to represent a given image sparsely. One-dimensional filter banks are traditionally applied to vertical and horizontal directions separately. Although this separable approach is quite simple, the performance of the 2-D system is relying on limited bandwidth of memory for representing intermediate results. Previously, we have developed filter banks in an non-separable manner because of the demands for high-performance image processing [3].

The two-dimensional discrete wavelet transform is versatile image processing instrument. It is employed in several image-compression standards (e.g. JPEG 2000) [4]. Whereas, the separable lifting scheme exhibits the smallest number of operations, and, on the contrary, require auxiliary memory to represent intermediate results [5].

II. LINEAR PHASE OF QUATERNIONIC FILTER BANK

As shown in [6], quaternions are especially suited to the parameterization of 4×4 orthogonal matrices. Namely, every matrix belonging to $SO(4)$, can be represented as a product of left and right unit quaternions P and Q ($|P| = 1$ and $|Q| = 1$) $\underset{\mathbf{R}\in SO(4)}{\forall} \; \underset{P,Q\in \text{unit quat.}}{\exists} \; \mathbf{R} = \mathbf{M}^{+}(P) \cdot \mathbf{M}^{-}(Q) = \mathbf{M}^{-}(Q) \times \times \mathbf{M}^{+}(P)$ directly (contrary to Givens rotations) to preserve their orthogonality in spite of quantization. A quaternionic critically sampled linear phase (LP) with pairwise-mirror-image (PMI) symmetric frequency responses paraunitary filter bank (PMI LP PUFB) results from substitution ($\mathbf{E}(z)$ is paraunitary polyphase transfer matrices of an analysis filter bank) [6], [7], assuming M as channel number:

$$\mathbf{E}(z) = \mathbf{G}_{N-1}\mathbf{G}_{N-2}\dots\mathbf{G}_1\mathbf{E}_0, \tag{1}$$

$$\mathbf{E}_0 = \tfrac{1}{\sqrt{2}}\mathbf{\Phi}_0\mathbf{W}\operatorname{diag}\left(\mathbf{I}_{M/2}, \mathbf{J}_{M/2}\right),$$

$$\mathbf{G}_i = \tfrac{1}{2}\mathbf{\Phi}_i\mathbf{W}\mathbf{\Lambda}(z)\mathbf{W}, \;\; i = \overline{1, N-1},$$

$$\mathbf{W} = \begin{bmatrix}\mathbf{I}_{M/2} & \mathbf{I}_{M/2}\\ \mathbf{I}_{M/2} & -\mathbf{I}_{M/2}\end{bmatrix}; \; \mathbf{\Lambda}_M(z) = \operatorname{diag}\left(\mathbf{I}_{M/2}, z^{-1}\mathbf{I}_{M/2}\right),$$

where N is order of the factorization; $\mathbf{I}_{M/2}$ and $\mathbf{J}_{M/2}$ denote the $M/2 \times M/2$ identity and reversal matrices, respectively; $\mathbf{\Gamma}_{M/2}$ is diagonal matrix which elements are defined as $\gamma_{mm} = = (-1)^{m-1}$, $m = \overline{1, M-1}$.

A 4-channel PMI LP Q-PUFB realized according to the fallows factorization of the matrices $\mathbf{\Phi}_i$ and $\mathbf{\Phi}_{N-1}$ [6]:

$$\mathbf{\Phi}_i = \mathbf{M}^{+}(P_i), \tag{2}$$

$$\mathbf{\Phi}_{N-1} = \mathbf{M}^{+}(P_i) \cdot \operatorname{diag}\left(\mathbf{J}_{M/2} \cdot \mathbf{\Gamma}_{M/2}, \mathbf{I}_{M/2}\right). \tag{3}$$

The matrices $\mathbf{M}^{+}(P)$ and $\mathbf{M}^{-}(Q)$ are left and right 4 by 4 multiplication matrices, accordingly: $Qx = \mathbf{M}^{+}(Q)\,x$, $xQ = \mathbf{M}^{-}(Q)\,x$; $P = p_1 + p_2 i + p_3 j + p_4 k$ and $Q = q_1 + + q_2 i + q_3 j + q_4 k$ are unit quaternions, where the orthogonal imaginary numbers obey the following multiplicative rules: $i^2 = j^2 = k^2 = ijk = -1$, $ij = -ji = k$, $jk = -kj = i$, $ki = -ik = j$.

The corresponding factorization of the matrices $\boldsymbol{\Phi}_i$ and $\boldsymbol{\Phi}_{N-1}$ for an 8-channel PMI LP Q-PUFB is shown below [7]:

$$\begin{aligned}\boldsymbol{\Phi}_i = \mathrm{diag}\left(\boldsymbol{\Gamma}_{M/2}, \mathbf{I}_{M/2}\right) \cdot \begin{bmatrix} \mathbf{M}^-(Q_i) & \mathbf{0}_{M/2} \\ \mathbf{0}_{M/2} & \mathbf{M}^-(Q_i) \end{bmatrix} \times \\ \times \begin{bmatrix} \mathbf{M}^+(P_i) & \mathbf{0}_{M/2} \\ \mathbf{0}_{M/2} & \mathbf{M}^+(P_i) \end{bmatrix} \cdot \mathrm{diag}\left(\boldsymbol{\Gamma}_{M/2}, \mathbf{I}_{M/2}\right),\end{aligned} \tag{4}$$

$$\begin{aligned}\boldsymbol{\Phi}_{N-1} = \mathrm{diag}\left(\boldsymbol{\Gamma}_{M/2}, \mathbf{I}_{M/2}\right) \cdot \begin{bmatrix} \mathbf{M}^-(Q_i) & \mathbf{0}_{M/2} \\ \mathbf{0}_{M/2} & \mathbf{M}^-(Q_i) \end{bmatrix} \times \\ \times \begin{bmatrix} \mathbf{M}^+(P_i) & \mathbf{0}_{M/2} \\ \mathbf{0}_{M/2} & \mathbf{M}^+(P_i) \end{bmatrix} \cdot \mathrm{diag}\left(\boldsymbol{\Gamma}_{M/2}, \mathbf{I}_{M/2}\right),\end{aligned} \tag{5}$$

where $\mathbf{0}_{M/2}$ is zero matrix size of $(M/2, M/2)$.

A. Non-separable LP PMI Q-PUFB

The direct implementation of multidimensional filter bank compatible with existing image standards is essential task [8]. Two-dimensional separable transform of image signal when the analysis PMI LP PUFB matrix $\mathbf{E}(z)$ is applied to a 2-D input signal $\mathbf{x}_{n,n}$ in horizontal and vertical directions, the output $\mathbf{y}_{n,n}$ is expressed as:

$$\begin{aligned}\mathbf{y}_{n,n} = \mathbf{E}(z) \cdot \mathbf{x}_{n,n} \cdot \mathbf{E}(z)^T = \mathbf{G}_{N-1}(z) \cdot \ldots \cdot \mathbf{G}_1(z) \cdot \mathbf{E}_0 \times \\ \times \mathbf{x}_{n,n} \cdot \mathbf{E}_0^T \cdot \mathbf{G}_1^T(z) \cdot \ldots \cdot \mathbf{G}_{N-1}^T(z).\end{aligned}$$

Based on the [3], [9] 2-D non-separable transformation result $\mathbf{y}_{n,n}$ can be represented as vector:

$$\begin{aligned}\mathbf{y}_{n^2,1} = \ddot{\mathbf{E}}(z)\mathbf{x}_{n\cdot n,1} = \ddot{\mathbf{G}}_{N-1}(z) \cdot \ldots \cdot \ddot{\mathbf{G}}_1(z)\ddot{\mathbf{E}}_0\mathbf{x}_{n^2,1}, \\ \ddot{\mathbf{E}}_0 = \tfrac{1}{2} \cdot \ddot{\boldsymbol{\Phi}}_0 \cdot \ddot{\mathbf{W}} \cdot \mathfrak{D}\left(\mathrm{diag}\left(\mathbf{I}_{M/2}, \mathbf{J}_{M/2}\right)\right) \times \\ \times \mathbf{P} \cdot \mathfrak{D}\left(\mathrm{diag}\left(\mathbf{I}_{M/2}, \mathbf{J}_{M/2}\right)\right) \cdot \mathbf{P},\end{aligned} \tag{6}$$

$$\begin{aligned}\mathbf{G}_i(z) = \tfrac{1}{4} \cdot \ddot{\boldsymbol{\Phi}}_i \cdot \ddot{\mathbf{W}} \cdot \ddot{\boldsymbol{\Lambda}}(z) \cdot \ddot{\mathbf{W}}; \\ \ddot{\mathbf{W}} = \mathfrak{D}(\mathbf{W}) \cdot \mathbf{P} \cdot \mathfrak{D}(\mathbf{W}) \cdot \mathbf{P}, \\ \ddot{\boldsymbol{\Lambda}}(z) = \mathfrak{D}(\boldsymbol{\Lambda}(z)) \cdot \mathbf{P} \cdot \mathfrak{D}(\boldsymbol{\Lambda}(z)) \cdot \mathbf{P}.\end{aligned}$$

where $\mathfrak{D}(\mathbf{W})$ denotes the matrix with n transform matrices $\mathbf{W}_{n,n}$ on the main diagonal, i.e. $\mathfrak{D}(\mathbf{W}) = \mathbf{I}_n \otimes \mathbf{W}_{n,n}$, where $\otimes$ is Kronecker product; upper double dots $\ddot{}$ denotes the 2D transformation matrix size $n^2 \times n^2$; $\mathbf{P}$ is the permutation matrix.

The corresponding two dimensional analogues of the matrices $\boldsymbol{\Phi}_i$ (4) and $\boldsymbol{\Phi}_{N-1}$ (5) for **8-channel analysis** PMI LP Q-PUBF is shown below:

$$\begin{aligned}\ddot{\boldsymbol{\Phi}}_i = \ddot{\mathbf{S}}_2 \cdot \ddot{\mathbf{M}}^+(Q_i) \cdot \mathbf{P} \cdot \ddot{\mathbf{M}}^+(Q_i) \times \\ \times \mathbf{P} \cdot \ddot{\mathbf{M}}^+(P_i) \cdot \mathbf{P} \cdot \ddot{\mathbf{M}}^+(P_i) \cdot \mathbf{P} \cdot \ddot{\mathbf{S}}_2, \\ \ddot{\boldsymbol{\Phi}}_{N-1} = \ddot{\mathbf{S}}_3 \cdot \ddot{\mathbf{M}}^-(Q_{N-1}) \cdot \mathbf{P} \cdot \ddot{\mathbf{M}}^+(Q_{N-1}) \cdot \mathbf{P} \times \\ \times \ddot{\mathbf{M}}^-(P_{N-1}) \cdot \mathbf{P} \cdot \ddot{\mathbf{M}}^+(P_{N-1}) \cdot \mathbf{P} \cdot \ddot{\mathbf{S}}_2, \\ \ddot{\mathbf{M}}_d^{\pm}(P) = \mathfrak{D}\left(\mathrm{diag}\left(\mathbf{M}^{\pm}(P), \mathbf{M}^{\pm}(P)\right)\right), \\ \ddot{\mathbf{S}}_2 = \mathfrak{D}(\mathbf{S}_2) \cdot \mathbf{P} \cdot \mathfrak{D}(\mathbf{S}_2) \cdot \mathbf{P}; \\ \mathbf{S}_2 = \mathrm{diag}\left(\boldsymbol{\Gamma}_{M/2}, \mathbf{I}_{M/2}\right), \\ \ddot{\mathbf{S}}_3 = \mathfrak{D}(\mathbf{S}_3) \cdot \mathbf{P} \cdot \mathfrak{D}(\mathbf{S}_3) \cdot \mathbf{P}; \\ \mathbf{S}_3 = \mathrm{diag}\left(\mathbf{J}_{M/2}, \mathbf{I}_{M/2}\right).\end{aligned} \tag{7}$$

Polyphase representation of $\mathbf{E}(z)$ after applying (7) implements 2-D non-separable PMI LP Q-PUFB, further denoted by the shorter abbreviation 2-D NSQ-PUFB.

III. Generalized image compression model

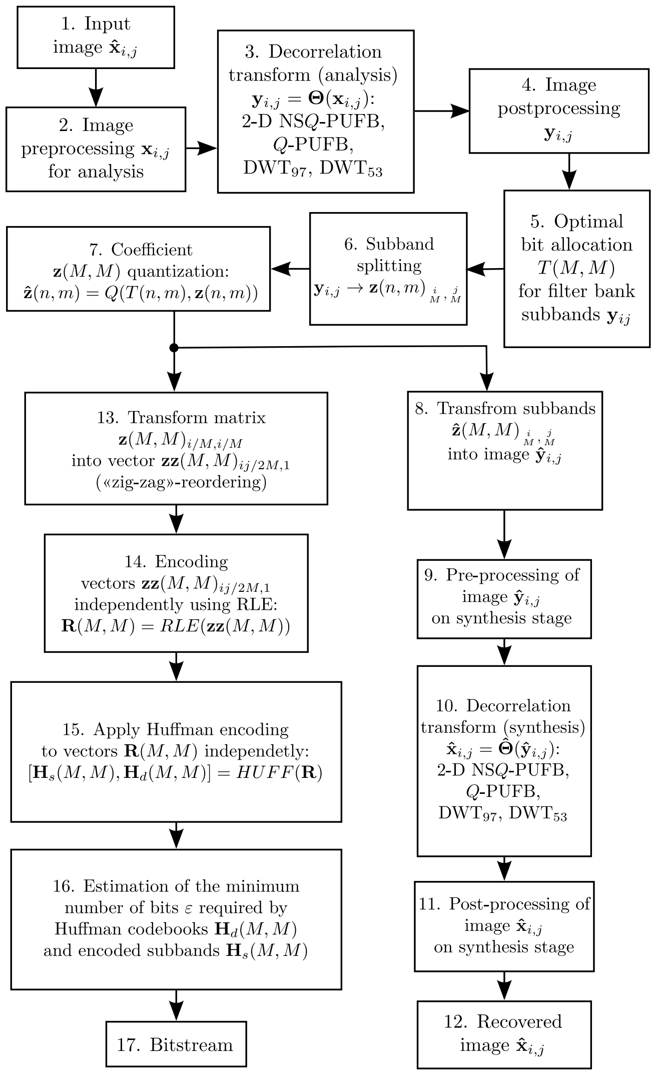

Fig. 1. Simplified image compression model

For experimental research in rate-distortion performance, generalized transform-based image compression model is required to evaluate performance of discussed transforms [10]. Evaluation model steps (data flow is depicted on fig. 1):

1) Test 8-bit image $\mathbf{x}_{i,j}$ used as input of image coder. For test used grayscale images from USC-SIPI Image Database [1]: Lena, Barbara, Pepper (resolution 512×512 pixels).
2) Preprocessing of the image $\mathbf{x}_{i,j}$ size of $i \times j$ pixels on the analysis stage 2-D NSQ-PUFB, is conversion 8×8 blocks to vectors (6).

[1]http://sipi.usc.edu/database/

$$\begin{matrix} 2.5 & 1.3 & 1.0 & 0.8 \\ 1.4 & 1.8 & 0.95 & 0.7 \\ 1.1 & 0.9 & 1.1 & 0.5 \\ 0.85 & 0.5 & 0.4 & 0.4 \end{matrix} \longrightarrow \begin{matrix} 2.5-1.3-1.4-1.1-1.8-1.0-0.8-0.95 \\ 0.9-0.85-0.5-1.1-0.7-0.5-0.4-0.4 \end{matrix}$$

Fig. 2. Example of *zigzag*-reordering for 4×4 block

3) Generalized decorrelation transform $\mathbf{y}_{i,j} = \mathbf{\Theta}(\mathbf{x}_{i,j})$:
   - ***Q*-PUFB**. The tile $\mathbf{x}_{i,j}$ comes to the first 2-D phase, which execute 1-D transform $\mathbf{\Theta}$ along rows i matrix $\mathbf{x}$ with 8-channel *Q*-PUFB. Next, second 1-D phase $\mathbf{\Theta}$ transform the columns of the j matrix with 8-channel *Q*-PUFB.
   - **DWT$_{97}$, DWT$_{53}$**. The tile $\mathbf{x}_{i,j}$ processed with 2-D transform, which consists two 1-D horizontal and vertical, applied by $\mathbf{\Theta}$ to rows i and columns j of $\mathbf{x}$. Subbands (LL, LH, HL, HH) after DWT are processed input images again until number of total subbands is equal 64 [11].
   - **2-D NS*Q*-PUFB**. 1-D vectors size of 64×1 from step 2 pass directly to 2-D NS*Q*-PUFB, which returns 2-D image $\mathbf{y}_{i,j}$ after 1 pass.
4) Postprocessing of image $\mathbf{y}_{i,j}$ at the analysis stage is deinterleave of coefficients and formatting subband images $\mathbf{y}(n,m)$.
5) Optimal bit allocation $T(M,M)$ in subbands $\mathbf{y}(n,m)$, whose purpose is to minimize the variance of the signal recovery error σ_r^2 with a limit on the shared bit resource [12].

$$b_k = b + \frac{1}{2}\log_2 \frac{\epsilon_k \sigma^2_{V_k}}{\prod_{k=0}^{64}(\epsilon_k \sigma^2_{V_k})^{\frac{1}{64}}}, \tag{8}$$

   where $\epsilon_k = \frac{1}{12}$, $V_k(n)$ is subband coefficients ($k = = \overline{1,64}$), b_k denotes predicted bit-budget for subband $V_k(n)$, $\sigma^2_{V_k}$ is dispersion of $V_k(n)$, b – total bit budget for all 64 subbands $V_k(n), k = 1,\ldots,64$.
6) Splitting image $\mathbf{y}_{i,j}$ for 64 subimages $\mathbf{z}(M,M)$ with $\frac{i}{M} \times \frac{j}{M}$ pixels.
7) Subband quantization $\mathbf{z}(M,M)$ using bit budget $T(M,M)$: $\hat{\mathbf{z}}(n,m) = Q(T(n,m), \mathbf{z}(n,m))$, where $Q(\cdot)$ is Lloyd-Max quantizer.
8) Merging subband images $\hat{\mathbf{z}}(M,M)_{\frac{i}{M},\frac{j}{M}}$ into $\hat{\mathbf{y}}_{i,j}$.
9) Preprocessing of image $\hat{\mathbf{y}}_{i,j}$ at synthesis stage is equal inverse step 4, i.e. represent values in 2-D interleave
10) Inverse decorrelation transform $\hat{\mathbf{x}}_{i,j} = \hat{\mathbf{\Theta}}(\hat{\mathbf{y}}_{i,j})$: *Q*-PUFB, 2-D NS*Q*-PUFB, DWT$_{97}$, DWT$_{53}$.
11) Postprocessing of image $\hat{\mathbf{x}}_{i,j}$ at synthesis stage of 2-D NS*Q*-PUFB is equal to transforming vectors size of 64×1 to 8×8 blocks.
12) Recovered image $\hat{\mathbf{x}}_{i,j}$.
13) Zig-zag reordering: transforming matrix $\mathbf{z}(M,M)_{i/M,i/M}$ to vector $\mathbf{zz}(M,M)_{ij/2M,1}$, example of process depicted on fig. 2.
14) Run-length encoding of vectors $\mathbf{zz}(M,M)_{ij/2M,1}$: $\mathbf{R}(M,M) = RLE(\mathbf{zz}(M,M))$, principle depicted on fig. 3.

$$2.5-0-0-1-1-0-0-0-0-0 \longrightarrow (2.5,1)-(0,2)-(1,2)-(0,5)$$

Fig. 3. Example of *RLE*-encoding

15) Huffman coding of vectors $\mathbf{R}(M,M)$
16) Estimation of minimal valuable bits ε required for codebook $\mathbf{H}_d(M,M)$ and $\mathbf{H}_s(M,M)$.
17) Complete bit-stream required suitable to decompression.

IV. Design example and experimental results

Using proposed model in sec. III of image compression pipeline, performance of following transform were evaluated in lossy scenario: 2-D NS*Q*-PUFB ($N = 3$), 1-D *Q*-PUFB ($N = 3$), DWT$_{97}$, DWT$_{53}$. Magnitude, phase and impulse responses of 1-D *Q*-PUFB depicted on fig. 4. Magnitude response of 2-D NS*Q*-PUFB and quatenions coefficients presented at fig. 5, results of rate distortion ratio for test images "Lena", "Barbara" and "Pepper" presented in tables III. Distortion estimated in PSNR, SSIM and DSSIM metrics. All filter bank coefficients are presented in table I

TABLE I
Coefficients of 1-D Q-PUFB ($N = 3$, $CG = 9.34$ dB) and 2-D NSQ-PUFB ($N = 3$, $CG_{2D} = 17.097$ dB)

Filter bank	q	$Re(q)$	$Im_i(q)$	$Im_j(q)$	$Im_k(q)$
1-D *Q*-PUFB	P_0	−0.79244	−0.10529	0.55207	0.23697
	P_1	−0.11637	0.97260	0.19568	−0.04706
	P_2	−0.65744	−0.47760	−0.01551	0.58259
	Q_0	0.92594	−0.01690	−0.37728	0.00270
	Q_1	−0.99551	0.06544	−0.01812	−0.06587
	Q_2	−0.42846	0.05721	−0.89764	0.08594
2-D NS*Q*-PUFB	P_0	−0.772903	0.514833	0.365746	0.061629
	P_1	−0.013821	−0.845056	−0.000859	−0.534499
	P_2	0.796620	0.600623	0.066466	0.015173
	Q_0	−0.812960	−0.494552	−0.288823	0.105334
	Q_1	0.921013	−0.015909	−0.386573	−0.045197
	Q_2	−0.017809	0.689550	−0.668783	−0.277367

Comparison of different image and video compression standards require equal bit-budget, which is hard or not even possible to implement. Spline approximation of rate-distortion curves [13], called Bjøntegaard delta, can be utilized for comparison of objective reconstruction quality (used PSNR and SSIM) on different bit-rates.

Analysis of objective results shows that best transform in given conditions is separable 1D *Q*-PUFB in terms of *PSNR* and *SSIM* for different *bpp*. Then, in descending order of quality of reconstruction: DWT$_{97}$, 2-D NS*Q*-PUFB and DWT$_{53}$. This is expected behavior in poor performance of lossless DWT$_{53}$, but DWT$_{97}$ is only lossy transform by design.

Comparison by metric ΔPSNR in the table II shown that 2-D NS*Q*-PUFB worser by approx. 1.66 dB than 1D *Q*-PUFB and 1.08 dB worser than DWT$_{97}$, close results by ΔSIMM shows that 2-D NS*Q*-PUFB worser by approx. 0.035 than 1D *Q*-PUFB and approx. 0.025 worser than DWT$_{97}$.

TABLE II
COMPARISON OF BJØNTEGAARD ΔPSNR

Transform A	Transform B	Test Image	ΔPSNR [dB]	ΔSSIM
2-D NSQ-PUFB	1-D Q-PUFB	Barbara	-2.0106	-0.0484
	DWT_{97}	Barbara	-1.4574	-0.0436
	DWT_{53}	Barbara	2.2846	0.0147
2-D NSQ-PUFB	1-D Q-PUFB	Lena	-1.6471	-0.0278
	DWT_{97}	Lena	-1.0272	-0.0185
	DWT_{53}	Lena	2.8304	0.0169
2-D NSQ-PUFB	1-D Q-PUFB	Pepper	-1.3173	-0.0284
	DWT_{97}	Pepper	-0.7737	-0.0116
	DWT_{53}	Pepper	2.2482	0.0346
1-D Q-PUFB	DWT_{97}	Barbara	0.4801	0.0079
	DWT_{53}	Barbara	4.2144	0.0710
1-D Q-PUFB	DWT_{97}	Lena	0.5825	0.0107
	DWT_{53}	Lena	4.5593	0.0491
1-D Q-PUFB	DWT_{97}	Pepper	0.5348	0.0177
	DWT_{53}	Pepper	3.6257	0.0652

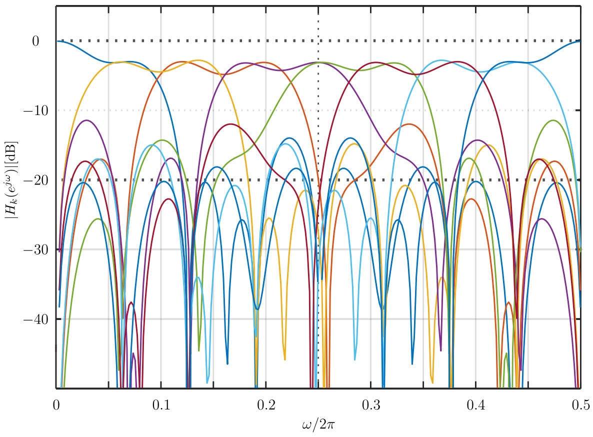

(a)

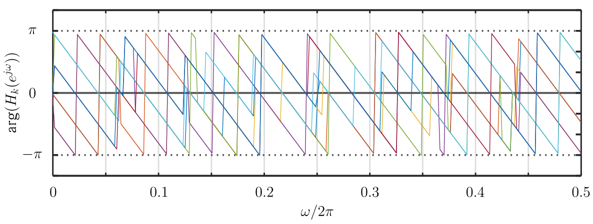

(b)

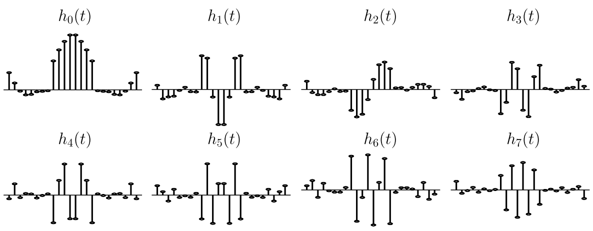

(c)

(a) – Magnitude response; (b) – Phase response; (c) – Impulse response.

Fig. 4. 8-channel (8×24) Q-PUFB

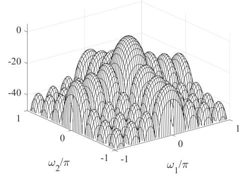

(a)

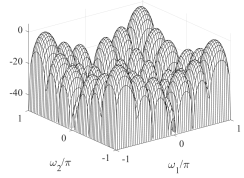

(b)

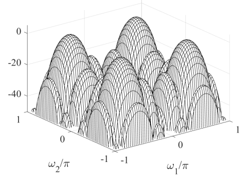

(c)

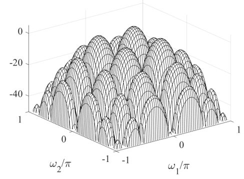

(d)

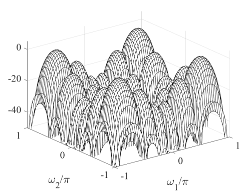

(e)

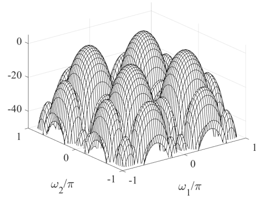

(f)

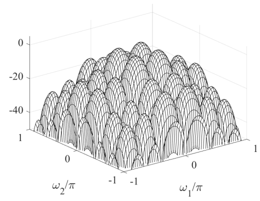

(g)

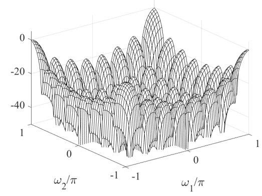

(h)

a – Channel $(1, 1)$; b – Channel $(2, 2)$; c – Channel $(3, 3)$; d – Channel $(4, 4)$; e – Channel $(5, 5)$; f – Channel $(6, 6)$; g – Channel $(7, 7)$; h – Channel $(8, 8)$

Fig. 5. Magnitude response of 2-D NSQ-PUFB

V. CONCLUSION

Rate-distortion estimated against PSNR, SSIM and DSSIM metrics, baseline image compression model is developed. According subjective comparison of recovered reference images for *bpp*: ≈ 0.25; ≈ 0.5; ≈ 1.0 shows no artifacts: Gibbs effect, undulating false circuits. The high frequency components, i.e. small details are well preserved.

In result 2-D NSQ-PUFB shows imperceptible different results in metrics SSIM by comparison with 1D Q-PUFB and DWT_{97}, but doesn't require auxiliary memory for intermediate results, which is important for high-performance VLSI and domain computing accelerators. Moreover, Q-PUFB integer implementations is compatible for both modes lossy and lossless, in comparison with lossless DWT_{53} and lossy DWT_{97} [9], [14].

TABLE III
RECOVERY RESULT FOR TEST IMAGES USING 2-D NSQ-PUFB

Image	bpp	Ratio	PSNR [dB]	SSIM	DSSIM
Lena	0.1359	58.867	28.507	0.48227	0.25887
	0.16852	47.473	29.493	0.54393	0.22803
	0.20068	39.864	30.415	0.58312	0.20844
	0.20068	39.864	30.415	0.58312	0.20844
	0.22469	35.604	30.9	0.6076	0.1962
	0.27552	29.036	31.71	0.64746	0.17627
	0.35336	22.64	32.937	0.6976	0.1512
	0.40285	19.859	33.656	0.72128	0.13936
	0.43849	18.244	34.126	0.74066	0.12967
	0.51085	15.66	34.983	0.77183	0.11409
	0.62896	12.719	36.104	0.8083	0.095851
	0.74537	10.733	37.264	0.83577	0.082115
	0.85159	9.3942	38.286	0.85926	0.070371
	0.95735	8.3564	38.985	0.87757	0.061216
Barbara	0.082378	97.113	22.502	0.32509	0.33745
	0.11069	72.273	23.087	0.38603	0.30699
	0.14339	55.79	23.881	0.46341	0.2683
	0.18731	42.709	24.838	0.552	0.224
	0.26566	30.114	26.594	0.65399	0.17301
	0.31247	25.603	27.331	0.68942	0.15529
	0.36421	21.965	27.886	0.71366	0.14317
	0.44207	18.097	28.845	0.74811	0.12594
	0.5705	14.023	30.334	0.79548	0.10226
	0.59274	13.497	30.742	0.80477	0.097616
	0.71256	11.227	32.043	0.83787	0.081063
	0.77372	10.34	32.737	0.84905	0.075474
	0.90195	8.8697	34.019	0.873	0.063498
	1.0863	7.3647	35.608	0.89745	0.051275
Pepper	0.1441	55.515	23.583	0.51836	0.24082
	0.17546	45.594	24.822	0.55421	0.2229
	0.21805	36.689	26.002	0.59807	0.20096
	0.27251	29.357	27.166	0.64628	0.17686
	0.30153	26.531	27.692	0.66972	0.16514
	0.3322	24.082	28.212	0.68646	0.15677
	0.37968	21.07	28.685	0.69799	0.151
	0.44316	18.052	29.373	0.71967	0.14017
	0.53728	14.89	30.598	0.76032	0.11984
	0.61963	12.911	31.468	0.7823	0.10885
	0.69893	11.446	32.266	0.79951	0.10024
	0.79842	10.02	33.07	0.81921	0.090395
	0.88818	9.0071	33.854	0.83536	0.082322
	1.0495	7.6227	35.204	0.86489	0.067554

REFERENCES

[1] K. R. Rao and P. Yip, *The Transform and Data Compression Handbook*. USA: CRC Press, Inc., 2018, 379 P.

[2] V. Strela, P. Heller, G. Strang, P. Topiwala, and C. Heil, "The application of multiwavelet filterbanks to image processing," *IEEE Transactions on Image Processing*, vol. 8, no. 4, pp. 548–563, 1999.

[3] N. A. Petrovsky, E. V. Rybenkov, and A. A. Petrovsky, "Two-dimensional non-separable quaternionic paraunitary filter banks," in *2018 Signal Processing: Algorithms, Architectures, Arrangements, and Applications (SPA)*, Poznan, Poland, sep 2018, pp. 120–125.

[4] M. Rabbani and R. Joshi, "An overview of the JPEG 2000 still image compression standard," *Signal Processing: Image Communication*, vol. 17, no. 1, pp. 3–48, 2002.

[5] H. Liao, M. Mandal, and B. Cockburn, "Efficient architectures for 1-D and 2-D lifting-based wavelet transforms," *IEEE Transactions on Signal Processing*, vol. 52, no. 5, pp. 1315–1326, 2004.

[6] M. Parfieniuk and A. Petrovsky, "Quaternionic building block for paraunitary filter banks," in *Proc. 12th European Signal Processing Conf. (EUSIPCO)*, Vienna, Austria, 6–10 Sep. 2004, pp. 1237–1240.

[7] ——, "Inherently lossless structures for eight- and six-channel linear-phase paraunitary filter banks based on quaternion multipliers," *Signal Process.*, vol. 90, pp. 1755–1767, 2010.

[8] M. Iwahashi and H. Kiya, "A new lifting structure of non separable 2D DWT with compatibility to JPEG 2000," in *2010 IEEE International Conference on Acoustics, Speech and Signal Processing*, 2010, 4 P.

[9] N. A. Petrovsky and E. V. Rybenkov, "2-D non-separable integer implementation of paraunitary filter bank based on the quaternionic multiplier block-lifting structure," in *IEEE 27th European Signal Processing Conference (EUSIPCO)*, sep 2019, 4 P.

[10] V. Goyal, "Theoretical foundations of transform coding," *IEEE Signal Processing Magazine*, vol. 18, no. 5, pp. 9–21, 2001.

[11] T. Acharya, *JPEG2000 standard for image compression: concepts, algorithms and VLSI architectures*. John Wiley & Sons, 2004, 273 P.

[12] N. A. Petrovsky, "Optimal bit allocation in the paraunitary subband image coder based on the quaternion algebra," *Doklady BGUIR*, vol. 79, no. 1, pp. 72–77, 2014.

[13] G. Bjøntegaard, "Calculation of average PSNR differences between RD-curves (VCEG-M33)," in *VCEG Meeting (ITU-T SG16 Q. 6)*, 2001, pp. 2–4.

[14] C. Zhang, C. Wang, and M. O. Ahmad, "A pipeline VLSI architecture for fast computation of the 2-D discrete wavelet transform," *IEEE Transactions on Circuits and Systems I: Regular Papers*, vol. 59, no. 8, pp. 1775–1785, Aug 2012.